Journal of Geophysical Research: Space Physics

RESEARCH ARTICLE
10.1029/2018JA025450

Key Points:
- TGF-associated RF pulses have a wide range of NLDN-estimated peak currents, which are proportional to their magnetic field peak amplitudes
- Median rise time and peak-to-zero time for TGF-simultaneous RF pulses were significantly longer than those for nonsimultaneous pulses
- A TGF that was associated with relatively high-power VHF radiation is described in detail

Supporting Information:
- Supporting Information S1

Correspondence to:
B. G. Mailyan,
bagrat.mailyan@uah.edu

Citation:
Mailyan, B. G., Nag, A., Murphy, M. J., Briggs, M. S., Dwyer, J. R., Rison, W., et al. (2018). Characteristics of radio emissions associated with terrestrial gamma-ray flashes. *Journal of Geophysical Research: Space Physics*, *123*. https://doi.org/10.1029/2018JA025450

Received 8 MAR 2018
Accepted 22 JUN 2018
Accepted article online 3 JUL 2018

Characteristics of Radio Emissions Associated With Terrestrial Gamma-Ray Flashes

B. G. Mailyan[1,2], A. Nag[1], M. J. Murphy[3], M. S. Briggs[2], J. R. Dwyer[4], W. Rison[5], P. R. Krehbiel[5], L. Boggs[1], A. Bozarth[1], E. S. Cramer[2], O. J. Roberts[6], M. Stanbro[2], and H. K. Rassoul[1]

[1]Florida Institute of Technology, Melbourne, FL, USA, [2]The Center for Space Plasma and Aeronomic Research (CSPAR), The University of Alabama in Huntsville, Huntsville, AL, USA, [3]Vaisala Inc., Louisville, CO, USA, [4]Department of Physics and Space Science Center (EOS), University of New Hampshire, Durham, NH, USA, [5]New Mexico Institute of Mining and Technology, Socorro, NM, USA, [6]Universities Space Research Association, Huntsville, AL, USA

Abstract In this study, we analyze 44 terrestrial gamma-ray flashes (TGFs) detected by the Fermi Gamma-ray Burst Monitor (GBM) occurring in 2014–2016 in conjunction with data from the U.S. National Lightning Detection Network (NLDN). We examine the characteristics of magnetic field waveforms measured by NLDN sensors for 61 pulses that occurred within 5 ms of the start-time of the TGF photon flux. For 21 (out of 44) TGFs, the associated NLDN pulse occurred almost simultaneously with (that is, within 200 μs of) the TGF. One TGF had two NLDN pulses within 200 μs. The median absolute time interval between the beginning of these near-simultaneous pulses and the TGF flux start-time is 50 μs. We speculate that these RF pulses are signatures of either TGF-associated relativistic electron avalanches or currents traveling in conducting paths "preconditioned" by TGF-associated electron beams. Compared to pulses that were not simultaneous with TGFs (but within 5 ms of one), simultaneous pulses had higher median absolute peak current (26 kA versus 11 kA), longer median threshold-to-peak rise time (14 μs versus 2.8 μs), and longer median peak-to-zero time (15 μs versus 5.5 μs). A majority (77%) of our simultaneous RF pulses had NLDN-estimated peak currents less than 50 kA indicating that TGF emissions can be associated with moderate-peak-amplitude processes. The lightning flash associated with one of the TGFs in our data set was observed by a Lightning Mapping Array, which reported a relatively high-power source at an altitude of 25 km occurring 101 μs after the GBM-reported TGF discovery-bin start-time.

1. Introduction

Thunderstorms can produce bursts of gamma-rays, known as Terrestrial Gamma-ray Flashes (TGFs). TGFs are typically detected worldwide by satellite-based instruments (e.g., Briggs et al., 2010; Fishman et al., 1994; Marisaldi et al., 2010; Smith et al., 2005), but several ground-based (e.g., Bowers et al., 2017; Dwyer et al., 2004, 2012; Enoto et al., 2017; Hare et al., 2016; Tran et al., 2015) and one aircraft-based (Smith et al., 2011) observations have been made. Initially, TGFs were thought to be a high-altitude phenomenon occurring at 30–50 km associated with positive cloud-to-ground (CG) lightning (e.g., Fishman et al., 1994; Inan et al., 1996; Inan & Lehtinen, 2005). However, spectral analyses of TGFs revealed that their source altitudes are typically below 20 km (e.g., Dwyer & Smith, 2005; Mailyan et al., 2016). Also, studies have shown that TGFs can be associated with intracloud (IC) lightning (e.g., Cummer et al., 2005; Shao et al., 2010; Stanley et al., 2006; Williams et al., 2006).

The exact mechanism by which TGFs are produced is still a subject of debate. A leading hypothesis is that TGFs are produced by the Relativistic Runaway Electron Avalanche (RREA) (e.g., Dwyer, 2003; Gurevich et al., 1992) process with consequent bremsstrahlung photon emission occurring in the presence of thundercloud electric fields. However, key details of the physical processes associated with TGFs such as the size of the particle-acceleration region, the source of the energetic seed particles required by RREA, and current and charge-transfer characteristics remain unknown. Some models assume that particle acceleration takes place at the tips of lightning leaders (e.g., Carlson et al., 2009; Celestin & Pasko, 2011), while others consider the acceleration to occur in large-scale electric fields in thunderclouds (e.g., Dwyer, 2012; Moss et al., 2006).

Electric and magnetic field waveforms in the radio frequency (RF) range associated with TGFs have become an important tool for studying this atmospheric phenomenon. The two-dimensional source location of a TGF,

observed by the Gamma-ray Burst Monitor (GBM) on-board the low-Earth-orbiting Fermi satellite, is obtained by correlating the time-of-occurrence of the TGF with that of the associated RF emission reported by a lightning locating system (LLS) such as the Worldwide Lightning Location Network (WWLLN; e.g., Connaughton et al., 2010, 2013; Mezentsev et al., 2016). This narrows down the source location of a TGF from being anywhere within the footprint (a circular region with a radius of 800 km) of the GBM to a specific latitude and longitude. The uncertainty of this location depends upon the location accuracy of the LLS, which can range from a few to greater than 15 km for WWLLN (Mallick et al., 2014), a global long-range LLS operating in the very low frequency (VLF) range.

Connaughton et al. (2013) examined 601 TGFs reported by the Fermi-GBM in conjunction with WWLLN-geolocated VLF pulses and found that the rate of association between these two data sets depended strongly upon the duration of a TGF. Short-duration (less than 200 μs) TGFs were more likely to be associated with WWLLN RF pulses than longer duration TGFs. These short-duration TGFs had an average WWLLN-estimated far-field energy that was significantly higher than that for longer-duration TGFs. According to the model developed by Dwyer and Cummer (2013), shorter duration TGFs will produce VLF signatures with higher radiation field peaks, which are proportional to the time-derivative of the current moment produced by the electron avalanche. Connaughton et al. (2013) interpreted WWLLN-reported RF pulses occurring almost simultaneously (within 200 μs) with GBM-reported TGF photon-count peak-times to be the VLF signature of relativistic electrons and their resulting ionization. On the other hand, RF pulses occurring within a longer time-window of 20 ms of the TGF peak-times were thought to be produced by "related IC discharges" (Connaughton et al., 2013) occurring in the same thunderstorm system as the TGF. Such pulses could probably also be directly associated with the TGFs (e.g., Smith et al., 2016), but the exact nature of the relationship remains unknown.

Lu et al. (2010) examined Lightning Mapping Array (LMA) data for a TGF observed by the Reuven Ramaty High Energy Solar Spectroscopic Imager (RHESSI) spacecraft and showed that the gamma-rays were produced during the initial stage of an IC flash. The 2-ms timing uncertainty of RHESSI complicated the analysis. However, after taking this uncertainty into account, a high power LMA source was observed to occur a few milliseconds before the TGF. Cummer et al. (2011) examined two GBM-detected TGFs along with associated magnetic field signatures measured by sensors of the U.S. National Lightning Detection Network (NLDN) and VLF sensors installed in Durham, North Carolina (Duke University), and Melbourne, Florida (Florida Tech). The magnetic field pulse started 50 μs (±17 μs) before the start of one TGF, and in case of the other TGF, there were a pair of field pulses starting 10 μs (±18 μs) and 50 μs (±18 μs) after the TGF start-time. The timing uncertainties were mostly due to the unknown TGF source altitude. Cummer et al. (2014) analyzed two TGFs reported by the Fermi-GBM having durations of 44 and 34 μs, with the durations of the corresponding RF pulses reported by the NLDN being 46 and 33 μs, respectively. Both TGFs occurred within 10 μs of the start-time of these RF pulses. The TGFs and RF pulses were considered to be effectively simultaneous after taking into account uncertainties associated with the source locations of the TGFs. The NLDN-reported peak current for the first TGF was 120 kA. Cummer et al. (2014) estimated the peak current for the other TGF to be greater than 500 kA. They concluded that the high peak currents of these events could indicate that they were produced during the TGF-generating electron acceleration by the RREA process rather than during traditional lightning processes.

In this paper, we examine the characteristics of RF pulses geolocated by the NLDN associated with 44 TGFs reported by the Fermi-GBM between January 2014 and July 2016. Additionally, for one of these TGFs, we analyze in detail data from the Kennedy Space Center (KSC) LMA, NLDN, and NEXRAD (Next-Generation Radar) weather surveillance radar.

2. Instrumentation and Data

The GBM is an auxiliary instrument on-board the Fermi Gamma-ray Space Telescope comprising of two bismuth germanate (BGO) and 12 sodium iodide (NaI) detectors (Meegan et al., 2009). Particles with effective energy ranges of 10–1,000 keV and 0.2–40 MeV are measured by the sodium iodide (NaI) and BGO detectors, respectively. The timing precision of the measurements is 2 μs, while absolute accuracy is several microseconds. The broad energy range of the BGO detectors along with a low dead-time of 2.6 μs makes them well suited for studying submillisecond TGFs with energies of up to tens of MeV. The Fermi-GBM is capable of

measuring TGFs within a horizontal distance of up to about 800 km from the spacecraft's footprint (Briggs et al., 2013). After implementation of new "ground-search" algorithms in 2012, the TGF detection rate improved to about 800 events per year, making the GBM the most efficient current-generation TGF observatory (Briggs et al., 2013). The Fermi-GBM TGF catalog (e.g., Roberts et al., 2018) provides the photon counts per 2 μs for each of the two BGO detectors, cumulative photon counts for the 12 NaI detectors per 2 μs (10 μs if NaI detectors are saturated), spacecraft position, TGF start-time measured at the spacecraft altitude, and the duration of the discovery-bin. The discovery-bin is the time-window in the ground-search algorithm corresponding to the most significant joint Poisson probability of occurrence of the identified TGF (Briggs et al., 2013). The TGF start-time in the catalog is defined as the start-time of this discovery-bin. The discovery-bin start-time is generally a reasonable approximation for the TGF photon flux start-time, as shown in Figures S1 to S21 in the supporting information for a subset of 21 TGFs in our data set that occurred simultaneously (see section 3) with NLDN RF pulses.

The U.S. NLDN uses ground-based electric and magnetic field sensors operating in the predominantly low-frequency (LF) range (400 Hz to 400 kHz) to measure electromagnetic field changes produced by lightning discharges and geolocates these discharges using time-of-arrival and magnetic direction finding techniques (Cummins & Murphy, 2009; Nag et al., 2015). Note that while the frequency range of NLDN sensors overlaps with the ultralow frequency (ULF), VLF, LF, and medium-frequency (MF) domains, for simplicity, in this paper we refer to the signatures measured by these sensors as "LF signatures" or "LF pulses." In some cases, other types of atmospheric electrical discharges such as TGFs that may produce relatively high-amplitude LF signatures are detected and geolocated by the NLDN. In addition to the time (the start-time of the LF pulse) and two-dimensional location (along with an estimated location error) of the sources of these pulses, the NLDN also provides information on their polarity and peak current. Ionospheric reflections of pulses are identified and rejected by the NLDN's geolocation algorithm. Only sensors within 775 km of the location of a pulse-source are used in estimating the pulse's peak current. The NLDN's geolocation algorithm does not mix pulses of opposite polarities when it groups sensor data to geolocate a pulse-source. So all sensors, including the ones at longer distances from the source, have to report the same initial polarity for a particular pulse for them to be used in the geolocation of the pulse. Magnetic field LF waveform characteristics such as rise time and peak-to-zero time of pulses are reported by individual sensors and geolocated events are classified by the network as IC pulses or CG return strokes based on their waveform characteristics. After a network-wide upgrade in 2013, the NLDN IC flash detection efficiency is about 50% (Murphy & Nag, 2015). The detection efficiency for negative first strokes in the Gainesville, Florida, region was reported to be about 98%; the IC flash and CG return-stroke classification accuracy was reported to be 95% and 92%, respectively (Zhu et al., 2016a, 2016b). The location accuracy for CG strokes is expected to be about a few hundred meters (Nag et al., 2015). The polarity estimation accuracy of the NLDN for lightning electromagnetic pulses is close to 100% (Nag et al., 2015). In the south, the coverage region of the NLDN extends to (going from east to west) the Bahamas, northern Mexico, and northern Baja California, beyond which the detection efficiency of the network decreases.

As noted above, the NLDN reports various magnetic field waveform characteristics including the initial polarity of RF pulses measured by its sensors. The NLDN sensors sample lightning magnetic field waveforms at a variable sampling rate above the sensor threshold so that all the waveform details and parameters relevant to geolocation, lightning type classification, and other applications are retained in the waveforms (Cummins et al., 2012; Honma et al., 2013). Fine structures of lightning waveforms are retained for the initial rising portions of pulses (up to the initial peak or up to the last significant peak of the same polarity following the initial peak). Fine waveform features occurring after this are not necessarily retained unless their amplitudes are a significant fraction of the peak value. Also, data between the zero crossing of one polarity and sensor threshold of the opposite polarity are not measured (Hare et al., 2016). After the useful features are extracted from the waveforms, the waveforms are generally not stored and hence are not available for detailed visual inspection at a later time. Furthermore, the RF signatures associated with TGFs (e.g., Lyu et al., 2018) can be complicated and are not well characterized. So it is possible that the initial-polarity estimation for such signatures provided by the NLDN is affected by its measurement system. For example, a pulse with positive initial polarity followed by a relatively large negative polarity overshoot could be reported by the NLDN to be negative due to the initial positive-polarity peak being below the detection threshold of the reporting sensors. In this study, we note the percentage of negative polarity TGF-associated RF pulses that were reported by the NLDN. Further discussion on the interpretation of the polarity of TGF-associated RF pulses is found in section 5.

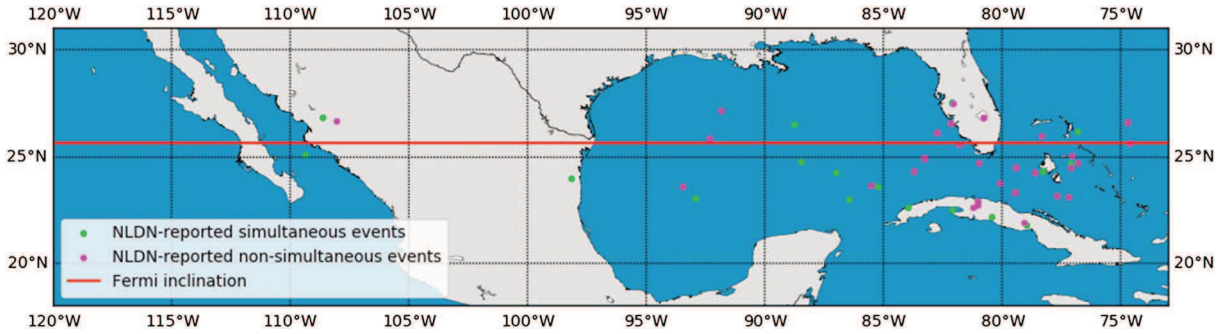

Figure 1. Map showing locations of 61 NLDN-reported events (RF pulses) that occurred within 5 ms of 44 TGFs reported by the Fermi-GBM. The green dots (NLDN-reported simultaneous events) indicate the locations of 22 pulses occurring within 200 μs of 21 TGFs. The pink dots (NLDN-reported nonsimultaneous events) indicate the locations of 39 pulses occurring in the 200-μs to 5-ms time window before or after the other 23 TGFs. The red line indicates the 25.6°N orbital inclination of Fermi. Note that some dots overlap with each other due to the spatial proximity of their locations.

The Fermi spacecraft has a low-Earth circular orbit. Its orbital inclination, which is the northernmost and southernmost latitude over which Fermi's footprint passes, is 25.6°. The 25.6°N latitude is indicated with a red line in Figure 1. TGFs that occur as far as a few hundred kilometers north of this latitude may be detected by the Fermi-GBM. For our analysis, we used a region (shown in Figure 1) over which we expect the coverage of the NLDN and the Fermi-GBM to overlap. In this region, we identified 44 GBM-reported TGFs occurring between January 2014 and July 2016 for which the NLDN geolocated one or more "lightning events" (RF pulses) occurring within 5 ms of the start-time of the TGF discovery-bin (or TGF start-time). There were 61 such NLDN-reported RF pulses of which 22 pulses occurred almost simultaneously (within 200 μs) with 21 TGFs. Note that, two NLDN-reported pulses occurred 5.0 μs before and 22 μs after the start-time of one of the TGFs (TGF09 in Table 1).

In Figure 1, we show the NLDN locations of the 61 RF pulses occurring within 5 ms of the TGF start-time. In order to account for the propagation delay between the locations of the TGF source and the spacecraft, a "light travel time correction" is applied to the spacecraft-reported times. To calculate this correction, we assume that the locations of these NLDN RF pulses are the two-dimensional locations of the TGF sources. This assumption is more robust if the RF pulses are signatures of the TGFs themselves rather than of lightning occurring in spatial and temporal proximity of these TGFs. See section 5 for further discussion. The altitude of the TGF sources is assumed to be 12 km. Then the distance between the TGF source locations and the spacecraft location is determined, from which the propagation delay is calculated (e.g., Briggs et al., 2010). Note that if this light travel time correction is not applied, timing errors of the order of a few milliseconds can occur. The two primary sources of error in the TGF-times computed using the above technique are (1) the assumption of a fixed TGF source altitude at 12 km and (2) the uncertainty associated with the two-dimensional NLDN-computed locations. These two errors are independent of each other. Assuming that TGF source locations can be at any altitude between 9 and 15 km, and using the 50% confidence (or error) ellipse semimajor and semiminor axis lengths computed by the NLDN, we estimate the median error range for the TGF-times computed by us to be about ±10 μs.

One of the TGFs in our data set (TGF09 in Table 1) occurred on 4 September 2015, and was located about 10 km south-east of Tampa, Florida. This region is covered by the KSC LMA. This LMA was installed in 2013, and in September 2015 (when TGF09 occurred) the LMA consisted of nine stations. The LMA geolocates in three-dimensions VHF sources associated with lightning discharges and provides information on their morphology and the thunderstorm charge structure (Krehbiel et al., 2000; Thomas et al., 2001). In addition to the source locations, the LMA data include information such as source power and a chi-square value that indicates the quality of a geolocation solution. Typically, for sources that are at relatively far distances (greater than 100 km or so from the closest sensor), source-altitudes tend to be overestimated (Boccippio et al., 2001; Thomas et al., 2004). We also examined NEXRAD data (e.g., Hall et al., 1984) measured at the Melbourne, Florida, Weather Forecasting Office and available every 5 min, for this TGF. Finally, atmospheric sounding data measured at Tampa, Florida, was analyzed to obtain information about the tropopause height. These data are available every 12 hr.

Journal of Geophysical Research: Space Physics

10.1029/2018JA025450

Table 1

Characteristics Reported by NLDN Sensors of 22 RF Pulses Occurring Simultaneously (Within 200 μs) With 21 TGFs Reported by the Fermi-GBM

TGF ID	Date (dd/mm/yy)	Time, UT (hh: mm: ss)	NLDN pulse start-time–GBM TGF start-time (μs)	Distance to NLDN sensor (km)	Peak current (kA)	NLDN-type classification	Rise time (RT) of magnetic field pulse (μs)	Peak-to-zero (PTZ) time of magnetic field pulse (μs)	Duration of initial "half-cycle" = RT + PTZ (μs)	Ratio of initial peak to opposite polarity overshoot of magnetic field pulse	Opposite polarity overshoot peak-to-zero time of magnetic field pulse (μs)
TGF01	10/5/14	7:01:02	42	498	44	CG	22	30	52	-	-
TGF02	4/8/14	8:29:34	162	590	−33	CG	12	30	42	-	-
TGF03	21/9/14	10:48:38	−23	589	205	IC	28	8.8	37	-	-
TGF04	24/9/14	8:35:48	−7.0	368	119	IC	23	11	34	-	-
TGF05	5/10/14	0:00:59	69	183	21	IC	20	12	32	-	-
TGF06	10/4/15	23:22:18	104	-	−47	CG	28	29	57	1.3	34
TGF07	12/7/15	21:24:05	73	437	24	CG	19	15	34	1.1	35
TGF08	29/8/15	20:52:46	174	372	20	CG	4.0	17	21	0.75	52
TGF09	4/9/15	21:23:43	−5.0	501	−13	CG	6.8	25	32	3.9	12
			22	69	38	CG	20	11	31	0.70	97
TGF10	5/9/15	19:24:50	3.4	728	77	CG	14	8.6	23	1.1	49
TGF11	24/9/15	10:49:14	26	368	166	CG	13	8.2	21	0.69	50
TGF12	1/11/15	13:44:13	−186	481	17	CG	15	21	35	0.49	30
TGF13	1/11/15	17:5:42	38	720	22	CG	9.2	15	24	1.6	27
TGF14	29/3/16	10:18:47	105	679	−23	CG	9.4	66	76	1.1	25
TGF15	22/5/16	4:49:12	97	497	24	CG	1.8	51	53	-	-
TGF16	20/6/16	10:59:10	35	143	17	IC	4.8	9.2	14	2.6	30
TGF17	8/7/16	5:40:06	60	191	128	CG	10	7.2	17	1.1	62
TGF18	15/7/16	22:58:44	13	595	31	CG	24	27	51	1.4	44
TGF19	18/7/16	23:57:41	−127	559	−15	CG	4.3	15	19	-	-
TGF20	22/7/16	21:34:04	200	655	−27	CG	18	27	45	0.69	35
TGF21	23/7/16	22:57:54	−21	551	22	CG	14	13	27	1.1	20
Arithmetic Mean	-	-	72	465	52	-	15	21	35	1.3	40
Median	-	-	50	498	26	-	14	15	33	1.1	35
Minimum	-	-	3.4	69	205	-	1.8	7.2	14	0.49	12
Maximum	-	-	200	728	13	-	28	66	76	3.9	97

Note. Statistics for all parameters are shown at the bottom of the table. Absolute values of the NLDN-TGF-time intervals (column 4) and peak currents (column 6) have been used to compute the respective statistics.

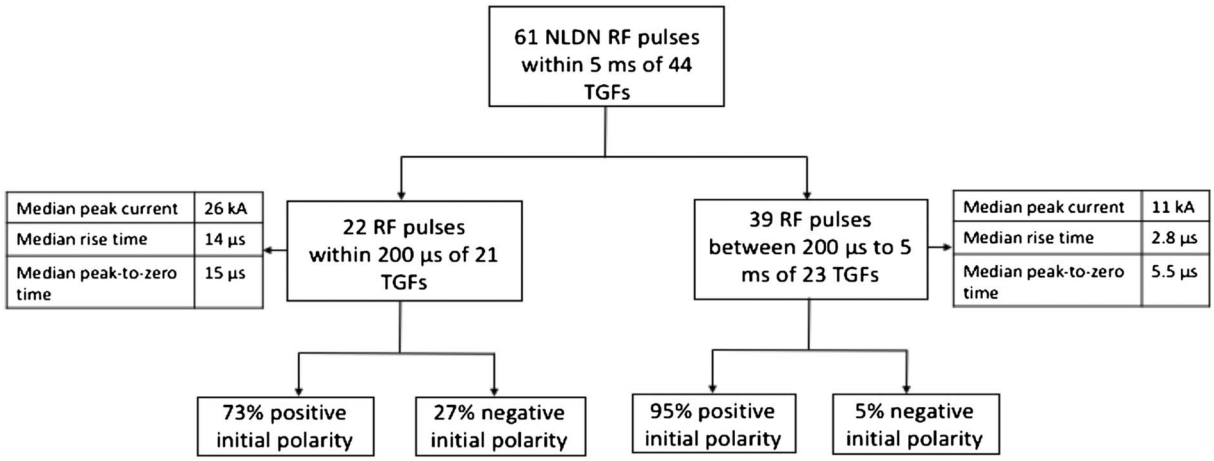

Figure 2. Schematic showing an overview of the NLDN-reported RF pulses associated with TGFs in our data set.

3. TGF-Associated Radio Frequency Pulses Observed by the NLDN

Figure 2 provides an overview of the NLDN RF pulses associated with TGFs in our data set. We examined the time interval between the NLDN-reported pulse start-time and the GBM-reported TGF start-time for 61 RF pulses associated with 44 TGFs. For 21 (34%) of the 61 RF pulses, the NLDN-reported start-time preceded the respective TGF's start-time reported by the GBM. The time intervals for those 21 pulses ranged from 5 μs to about 2.9 ms, with the median being 1.1 ms. For 40 RF pulses (about 66%) whose start-times were after the respective TGF's start-time, the time intervals ranged from 3 μs to 4.5 ms with the median being 401 μs. Twenty six (43%) of the 61 RF pulses were classified by the NLDN as CG strokes. Eight (13%) pulses had negative initial polarity. For 21 (48%) of the 44 TGFs, the start-times of one or two (for TGF09 only, as mentioned in section 2) RF pulses occurred nearly simultaneously (within 200 μs) with the respective TGF's start-time. For these TGFs, the median absolute time interval between the NLDN-reported pulse start-time and the respective TGF's start-time is 50 μs. Sixteen (73%) of these 22 RF pulses started after the TGF start-time. Eighteen (82%) of these 22 pulses were classified by the NLDN as CG strokes. Six (27%) of 22 pulses had negative initial polarity.

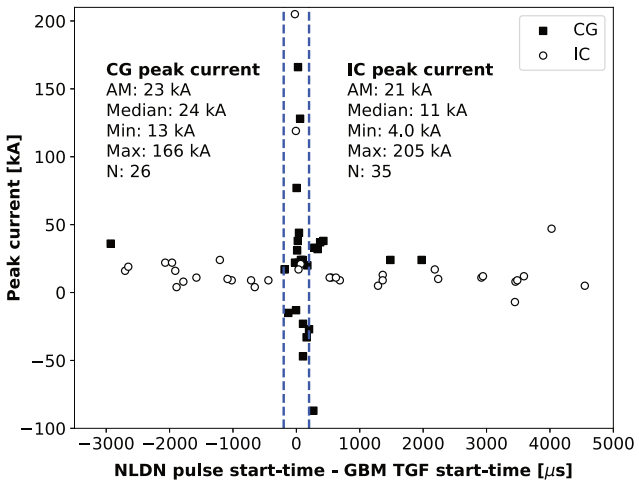

Figure 3. Scatter plot showing the NLDN-estimated peak currents for 61 RF pulses versus the NLDN-TGF time intervals. Pulses that were classified by the NLDN as CG strokes are shown using black squares, and those classified as IC pulses are shown using hollow circles. The vertical dashed lines indicate the 200-μs time-window within which RF pulses were considered to be essentially simultaneous with TGFs. The arithmetic mean (AM), median, minimum (Min), and maximum (Max) are shown for the absolute values of the peak currents.

Figure 3 shows the scatter plot of the NLDN-estimated peak currents for the 61 RF pulses versus the NLDN-TGF time intervals. Pulses that were classified by the NLDN as CG strokes are shown using black squares and those classified as IC pulses are shown using hollow circles. The NLDN-estimated peak currents can be viewed as a quantity proportional to the peak magnetic radiation field of these pulses. The NLDN classified 26 (43%) of the 61 pulses as CG, with the absolute values of peak currents ranging from 13 to 166 kA and the median being 24 kA. Thirty-five (57%) pulses were classified as IC, with their absolute peak-currents ranging from 4 to 205 kA and the median being 11 kA. For the 22 RF pulses that occurred nearly simultaneously with TGFs (200-μs time-window between the two vertical dashed lines in Figure 3), the absolute values of peak currents ranged from 13 to 205 kA, with the median being 26 kA. Seventeen (77%) of these pulses had peak currents less than 50 kA. The absolute values of peak currents for pulses that were not simultaneous with TGFs, but within 5 ms of one, ranged from 4 to 87 kA with the median being 11 kA. This median peak current is 2.4 times smaller than the median peak current of the simultaneous RF pulses. Eight (21%) out of 39 of these nonsimultaneous pulses were classified by the NLDN as CG. Two (5.1%) out of 39 pulses had negative initial polarity.

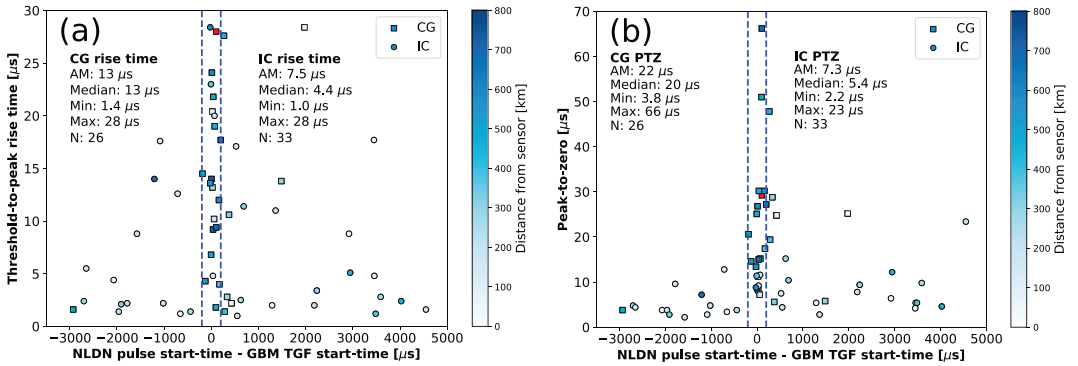

Figure 4. Scatter plot showing the (a) threshold-to-peak rise time (b) and peak-to-zero (PTZ) time for 59 RF pulses versus the NLDN-TGF time intervals. Note that for 2 out of the 61 RF pulses which were associated with the 44 TGFs in our data set, the threshold-to-peak rise times and peak-to-zero times were not available. Pulses that were classified by the NLDN as CG strokes are shown using squares and those classified as IC pulses are shown using circles. The circles and squares are color-coded by distance of pulse location from the sensor that measured the magnetic field waveform features, as indicated by the color bar on the right of the figure. One event (a CG stroke), for which the distance to sensor was not available is shown using a red square.

Figures 4a and 4b show the scatter plots of NLDN-reported magnetic field threshold-to-peak rise times and peak-to-zero times, respectively, for 59 RF pulses versus the NLDN-TGF time intervals. Note that for 2 out of 61 pulses, the threshold-to-peak rise times and peak-to-zero times were not available. Pulses that were classified by the NLDN as CG strokes are shown using squares and those classified as IC pulses are shown using circles. Additionally, the circles and squares are color-coded by distance of the pulse location from the sensor that measured the magnetic field waveform features, as indicated by the color bar on the right of the figure. As can be seen from Figure 4a, the threshold-to-peak rise times ranged from 1.4 to 28 μs with the median being 13 μs for 26 CG strokes, and for 33 IC pulses they ranged from 1.0 to 28 μs with the median being 4 μs. For the 22 RF pulses that occur nearly simultaneously with TGFs (shown between the two vertical dashed lines in Figure 4a), the threshold-to-peak rise times ranged from 1.8 to 28 μs, with the median being 14 μs. The threshold-to-peak rise times for pulses that were not simultaneous with TGFs, but within 5 ms of one, ranged from 1 to 28 μs with the median being 2.8 μs. From Figure 4b we can see that the peak-to-zero times ranged from 3.8 to 66 μs with the median being 20 μs for 26 CG strokes, and for 33 IC pulses they ranged from 2.2 to 23 μs with the median being 5 μs. For the 22 RF pulses that occur nearly simultaneously with TGFs (shown between the two vertical dashed lines in Figure 4b), the peak-to-zero times ranged from 7.2 to 66 μs, with the median being 15 μs. For pulses that were not simultaneous with TGFs, but within 5 ms of one, the peak-to-zero times ranged from 2.2 to 48 μs with the median being 5.5 μs.

From the above analysis we see that the median threshold-to-peak rise time and peak-to-zero time for NLDN-reported RF pulses occurring nearly simultaneously with TGFs were about a factor of 4 and 3 longer, respectively, than those for RF pulses that were not simultaneous with TGFs, but occurred within 5 ms of one. Since the NLDN uses waveform parameters and peak currents to classify pulses as IC or CG, and CG strokes tend to have longer rise times and peak-to-zero times and higher peak currents, this is likely why most RF pulses that were simultaneous with TGFs in our data set were classified by the NLDN as CG strokes. The NLDN, of course, assumes that all RF pulses it detects are from lightning, which is not correct for RF emissions from other sources such as TGFs. But regardless of their source, the magnetic field waveform characteristics of these RF pulses such as initial polarity, rise time, and peak-to-zero time measured by the NLDN sensors are still valid. On the other hand, the NLDN-estimated peak current, which is a model-dependent parameter rather than simply a waveform characteristic, is not valid for RF pulses emitted by sources other than CG strokes (see section 5 for further discussion). For such RF pulses, the NLDN peak current is simply an indication of their magnetic field peak amplitude.

The magnetic field rise times and peak-to-zero times discussed above will be affected by the propagation of electromagnetic waves over lossy soil from the source location to the measuring sensor, even though most of the events in our data set occurred over ocean (see Figure 1) and the propagation paths are predominantly over salt water (which has much higher conductivity than land). The horizontal distances between source locations and NLDN sensors that measured the waveforms were available for 58 out of 59 RF pulses for

which rise times and peak-to-zero times were measured, and these distances ranged from 25 to 728 km with the median being 286 km. The event for which distance to sensor was not available is a CG stroke and is shown using a red square in Figure 4. For this data set, we did not find a strong correlation between distance and threshold-to-peak rise time or between distance and peak-to-zero time, with the R^2 (correlation coefficient) value in each case being 0.04 and 0.18, respectively. This can be qualitatively observed from Figure 4, which shows both short and long rise times and peak-to-zero times being reported by sensors at farther distances (circles and squares with darker blue color). Note that the R^2 values are not shown in Figure 4.

Table 1 summarizes the characteristics reported by NLDN sensors of the 22 RF pulses that occurred simultaneously with 21 TGFs. The NLDN sensors that measured the waveforms were at horizontal distances ranging from 69 to 728 km with the median distance being 498 km. Of the six negative initial-polarity pulses, distance-to-sensors were available for five pulses and they ranged from 501 to 679 km. Relevant discussion on NLDN's geolocation and polarity- and peak current-estimation techniques can be found in section 2. In addition to the characteristics discussed above, the ratio of initial peak to opposite polarity overshoot and the opposite polarity overshoot peak-to-zero time for magnetic field pulses were each available for 15 pulses. The values of these parameters ranged from 0.49 to 3.9 and 12 to 97 μs, respectively, with the median values being 1.1 and 35 μs, respectively. We computed the duration of the initial "half-cycle" of these pulses, which is the sum of the threshold-to-peak rise time and the peak-to-zero time. These durations ranged from 14 to 76 μs, with the median being 33 μs.

4. TGF Observation on 4 September 2015

The Fermi-GBM off-line search algorithm (Briggs et al., 2013) identified a TGF (TGF09 in Table 1) within a discovery-bin of 70 μs occurring on 4 September 2015 at 21:23:43 UT. For this TGF, the GBM's two identical BGO detectors on opposite sides of the Fermi-spacecraft reported 6 and 10 photon counts, respectively, with energies above 200 keV for this TGF. These counts are relatively low compared to the average photon count of about 20 (Mailyan et al., 2016) for TGFs that trigger the GBM's on-board measurement system. Note that approximately 85% of TGFs are not initially reported by the on-board measurement system but are later identified by the off-line search algorithm. The 4 September 2015 TGF is not suitable for individual spectral analysis (e.g., Gjesteland et al., 2015; Mailyan et al., 2016) due to the low photon counts. However, RF emissions from this TGF were reported by several LLSs, (WWLLN, NLDN, GLD360, and KSC LMA), as shown in Figure 5.

We now examine in detail the characteristics of the RF emissions associated with TGF09 reported by LLSs. WWLLN reported an event about 42 μs after the TGF start-time and geolocated it at 27.5778° (latitude), and −82.0627° (longitude; shown using a star symbol in panels (a) and (d) of Figure 5), with an estimated location error of about 6.2 km. Note that the Fermi TGF catalog uses WWLLN to geolocate TGFs as discussed in section 2. For this event WWLLN estimated a far field VLF (between 5 and 18 kHz) energy of 1.7 kJ. Connaughton et al. (2013) reported a median energy of 3.1 kJ for WWLLN events occurring within 200 μs of GBM-reported TGFs and 700 J for the events occurring within 0.2–20 ms of TGFs. Our search of NLDN data revealed two events that were classified by the NLDN as CG strokes (shown using "x" symbols in panels (a) and (d) of Figure 5) occurring 5.0 μs before and 22 μs after the TGF-time, respectively, followed by two NLDN-reported IC pulses (shown using triangle symbols in Figure 5d) occurring about 0.5 ms and 270 ms after the TGF-time, respectively. No other strokes or pulses were reported by the NLDN within 10 km and 1 s of the first "CG stroke." The NLDN-reported peak currents for the two "CG strokes" were −13 and +38 kA, respectively, and for the two IC pulses were +11 and +2 kA, respectively. GLD360 geolocated one event (shown using a hollow-circle symbol in Figure 5d) with an estimated location error (given by the length of the semimajor axis of the 50% error ellipse) of 1.5 km occurring 28 μs after the TGF start-time and with a peak current of +67 kA. Table 1 shows the characteristics of the NLDN reported "CG strokes" associated with this TGF (TGF09), including magnetic field waveform features reported by individual NLDN sensors. The threshold-to-peak rise time and peak-to-zero time for the first (negative) "CG stroke," measured by a sensor at a distance of 501 km, were 6.8 and 25 μs, respectively, and those for the second (positive) "CG stroke," measured by a sensor at a distance of 69 km, were 20 and 11 μs, respectively. These two events were geolocated 1.9 km apart from each other with the estimated NLDN location errors (given by the length of the semimajor axis of the 50% error ellipse) being 2 and 0.3 km, respectively. The time interval between the start-times of the first and second pulse is 27 μs. Both

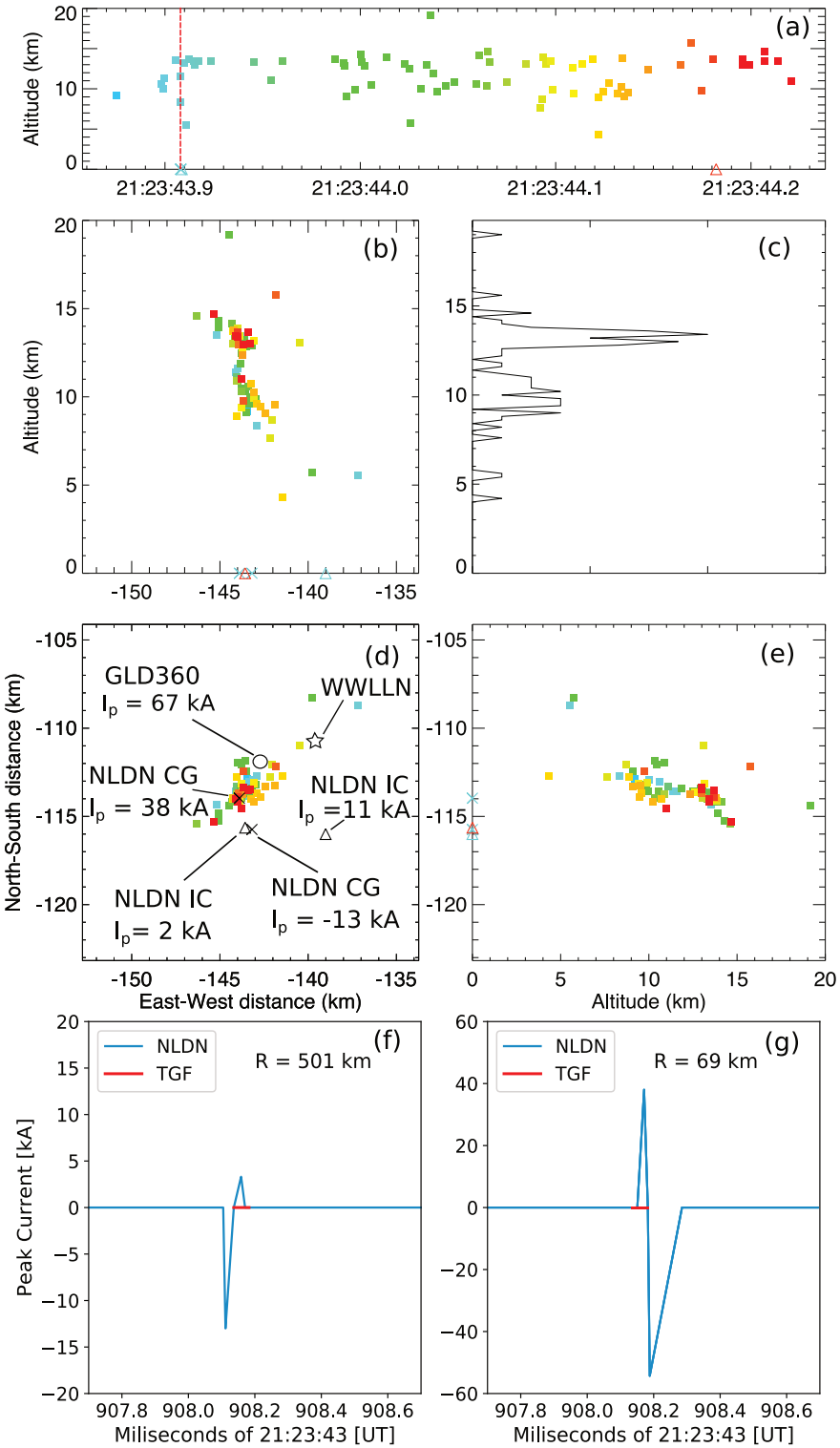

Figure 5. (a) Time versus altitude, (b) east-west distance versus altitude, (c) histogram of source altitudes, (d) east-west versus north-south distance, and (e) altitude versus north-south distance of VHF sources for the flash during which TGF09 (see Table 1) occurred. The red vertical line in (a) indicates the time of occurrence of the TGF. The LMA sources are color-coded by time. The X and triangle symbols indicate NLDN-reported CG and IC events, respectively. Only LMA sources with chi-square values less than 0.5 are included. See text for additional details. Also shown in (d) are the locations of lightning events reported by the NLDN, GLD360, and WWLLN. Reconstructed (using information in Table 1) "waveforms" for a (f) −13 kA and a (g) +38 kA NLDN-reported CG stroke occurring during this flash are shown. The NLDN sensors that recorded these waveforms were at distances of 501 and 69 km from the source locations, respectively. These "strokes" overlap in time with the Fermi-GBM photon counts. The time interval between the first and last photon counts is shown with a red line in (f) and (g).

these NLDN-reported "CG strokes" overlap in time with the Fermi-GBM photon counts, as shown in Figures 5f and 5g, using reconstructed (from NLDN-reported waveform characteristics shown in Table 1) "waveforms" in blue and the TGF duration (time interval between first and last photon counts) shown in red. Note that the vertical axis in panels (f) and (g) of Figure 5 is the NLDN-estimated peak current, which can be viewed as magnetic radiation field that has been distance normalized and appropriately scaled. The second pulse was reported to have a magnetic radiation field opposite polarity overshoot that was larger than the initial peak. This is rather unusual for a CG stroke measured at a distance of 69 km (see, for example, Lin et al., 1979 for typical returns stroke wave shapes at different distances). Additionally, it is unlikely for two CG strokes to occur just 1.9 km from and within 27 μs of each other. We speculate that these magnetic field pulses, classified by the NLDN as a "CG strokes," are, in fact, parts of the RF signature of TGF09 and could be associated with propagating relativistic electron beams generated by mechanisms discussed in Dwyer and Cummer (2013). Another possibility is that the RF signature could be of current traveling in conducting paths "preconditioned" by TGF-associated relativistic electron beams between cloud charge regions of opposite polarity. This +38 kA pulse reported to occur 22 μs after the TGF start-time by the NLDN is very likely the same one reported by GLD360, 28 μs after the TGF start-time with a peak current of +67 kA, and also by WWLLN, 42 μs after the TGF-time. Using the LMA data as ground-truth, due to the lack of VHF sources at altitudes below about 4 km as shown in Figure 5a, we conclude that the −13 and +38 kA pulses were actually produced by in-cloud sources and the NLDN misclassified them as CGs. Note that WWLLN and GLD360 did not report the −13 kA pulse preceding the TGF, likely due to the lower detection efficiencies of these long-range LLSs relative to the NLDN.

Figure 5a shows the time versus altitude of the LMA-reported VHF sources from the lightning flash during which TGF09 occurred, on a 380 ms timescale. In order to remove unreliably geolocated sources, we have excluded those that have geolocation solutions with chi-square values greater than 0.5 (Lu et al., 2010). These VHF sources are at a distance of roughly 180 km from the LMA, which could indicate that the reported altitude values are overestimated by about 3–4 km (Thomas et al., 2004, Figure B3). The four NLDN-reported events are shown on the horizontal axes in Figures 5a and 5b and on the vertical axis in Figure 5e. Note that three of these events that occur closely spaced in time toward the beginning of the flash overlap with each other in Figure 5a. Figure 5c shows the histogram of the source altitudes for 75 LMA sources. The histogram has two peaks at about 10 and 13.5 km with the median source altitude being 12.8 km. Note that a VHF source (not shown in Figure 5) with a relatively high chi-square value of 1.37 and coincident in time with the second NLDN-classified CG stroke was geolocated at a relatively-high altitude of about 25 km. The high chi-square value could indicate that the LMA location of this source is imprecise.

Figure 6a shows the east-west distance versus altitude of LMA-reported sources, like in Figure 5b, but for 85 sources with chi-square values of less than 1.5. Figures 6b–6d show, respectively, the chi-square, the two-dimensional distance from the NLDN-reported location of the +38 kA event (which is likely the TGF RF pulse), and the source power of VHF sources occurring in a 20-ms time-window centered around the occurrence time of the BGO-reported TGF-time. From Figure 6b we see that only the source geolocated by the LMA at 25 km altitude had chi-square value greater than one. This source occurred 101 μs after the BGO-reported TGF-time (discovery-bin start-time) and 31 μs after the TGF discovery-bin end-time. Two other VHF sources occurring 187 and 21 μs before the TGF-time were reported to have chi-square values of 0.07 and 0.24, respectively, and their altitudes were 11.6 and 8.3 km, respectively. Also, the two-dimensional distance of the VHF source at 25 km altitude from the location of the NLDN-reported RF pulse was 10.5 km, as seen in Figure 6c. Only one other VHF source in this 20-ms time-window had a distance greater than 5 km from the RF pulse, with all other sources being relatively close (less than 2 km distance). Finally, this relatively high-altitude VHF source had somewhat high peak radiated power of 20 dBW, compared to the median peak radiated power of 11 dBW for all VHF sources in the flash. In summary, the LMA geolocated a relatively high-power VHF source occurring almost simultaneously with the TGF at an altitude of 25 km, but it is likely that the estimated location (including the altitude) is somewhat unreliable due to the flash being roughly 180 km from the KSC LMA. If we assume that this high-power source was actually located at the preceding VHF source, the time interval between the high-power source and the GBM-reported TGF-start-time would be about 79 μs (versus 101 μs obtained using its original location).

We examined data from the NEXRAD dual polarization weather surveillance radar located in Melbourne, Florida. Figure 7 shows the base reflectivity for the 5-min interval between 21:21 UT and 21:26 UT, which

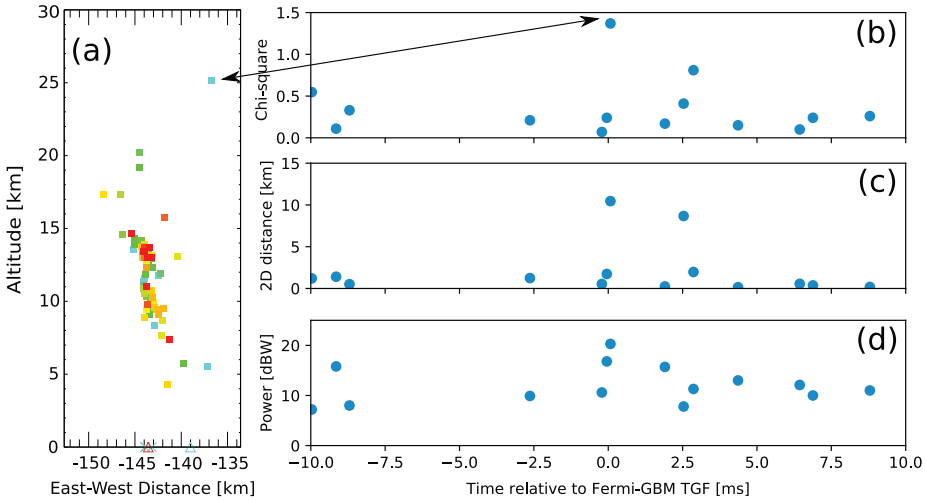

Figure 6. East-west distance versus altitude for LMA-reported sources, like in Figure 5b, but for 85 sources with chi-square values of less than 1.5. (b) Chi-square, (c) two-dimensional distance from the NLDN-reported location of the +38 kA event (which is likely the TGF RF pulse), and (d) source power of VHF sources occurring in a 20-ms time-window centered around the occurrence time of the BGO-reported TGF time. The VHF source at 25 km altitude is shown in (a) and the arrow points to that source with a chi-square of 1.37 in (b).

includes the TGF occurrence time of 21:23:43 UT. Also shown using white dots are the LMA VHF sources with chi-square values less than 0.5. The red line indicates the vertical locus of the two-dimensional position of the NLDN-geolocated +38 kA "CG stroke" occurring 22 μs after the TGF-time. The radar reflectivity shows an overshooting top reaching about 15 km, relatively close to where the NLDN event and VHF sources were located. Overshooting cloud tops (not necessarily spatially close to TGFs) in TGF-producing storms were reported by Chronis et al. (2015).

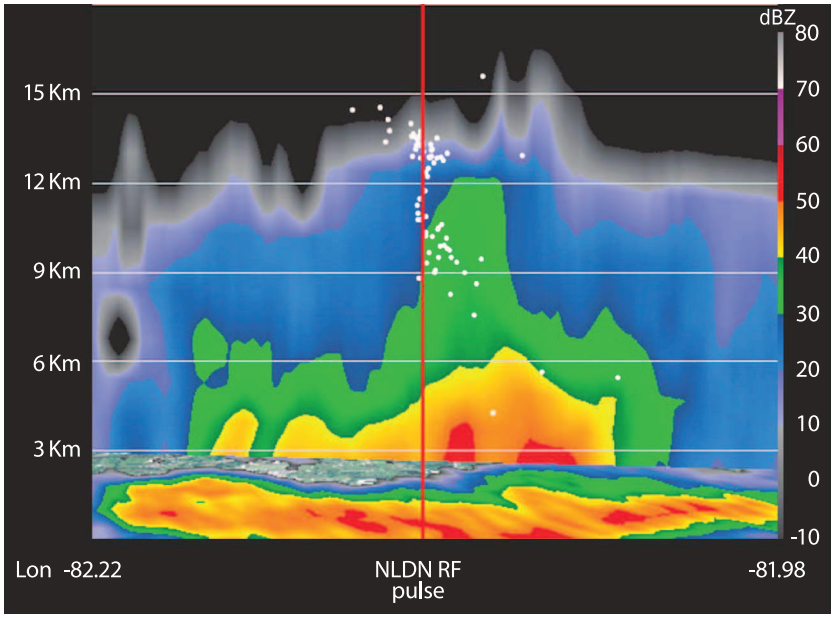

Figure 7. The base reflectivity from the NEXRAD weather radar located in Melbourne, Florida for the 5-min interval between 21:21 UT and 21:26 UT, which includes the occurrence time of TGF09 (21:23:43 UT). Also shown using white dots are the LMA VHF sources with chi-square values less than 0.5. The red line indicates the vertical locus of the two-dimensional position of the NLDN-geolocated +38 kA "CG stroke" occurring 22 μs after the TGF start-time.

We also examined radiosonde data, which is available every 12 hr from the Tampa Weather Forecasting Office (KTBW), for measurements performed on 4 September 2015 12:00 UT and 5 September 2015 00:00 UT (preceding and following the TGF-producing storm, respectively). In both cases the vertical temperature profile showed an inversion at altitudes of 16–17 km, which we infer to be the tropopause altitude. This is somewhat consistent with the observed VHF source altitudes which are as high as 19 km (for sources with chi-square less than 0.5).

An interesting feature of the reflectivity profile shown in Figure 7 is the relatively tall region with reflectivities of 30–40 dBZ (shown in green) between 6–12 km mean sea level (MSL) altitude. Generally speaking, this reflectivity range is typically characteristic of graupel at these altitudes, which were all above the environmental 0°C level at 4.9 km MSL (taken from the KTBW soundings at 12:00 and 00:00 UTC). The hydrometeor classification algorithm that is used with the dual-polarization NEXRAD data (described in Park et al., 2009) indicated mainly dry snow, rather than graupel, at altitudes above about 8 km (which corresponds to the 2.4° tilt angle of the radar) in this particular storm. A mixture of graupel and dry snow was indicated at the next lower tilt angle of 1.8°, which was roughly 6–7 km altitude in the vicinity of this storm. We do note, however, that the decision boundary between graupel and dry snow lies in the low to mid-30s of dBZ in reflectivity wherever the differential reflectivity is less than or equal to 1.5 dB and the horizontal-vertical correlation coefficient is at least 0.9, conditions that apply to the high reflectivity column in this storm (except in areas of range folding, which were indicated at higher tilts from the KMLB radar data near this storm). Also, dry snow is not very reflective unless large aggregates of it are present, which is not very likely in a strongly convective, highly electrified storm. Thus, it is likely that at least a portion of the high-reflectivity column between roughly 8–12 km in Figure 7, in fact, is graupel.

The dominant charge on this column of graupel/dry snow is expected to be determined by the noninductive, relative growth rate charging mechanism, which has been extensively reviewed by Saunders (2008). The laboratory charging studies reviewed by Saunders indicate that graupel receives negative charge at temperatures lower than about −10 to −15°C, depending on the effective water content of the cloud and the conditions in which the small ice crystals grow. In the KTBW soundings from this storm, those temperatures corresponded to altitudes between approximately 6.5 and 7.5 km MSL. Thus, it is reasonable to suggest that the high-reflectivity column, at least for altitudes 7.5 km and above in Figure 7, was probably dominated by negative charge. This is supported by the vertical distribution of the LMA data shown in Figure 5c. Noisier VHF emissions tend to occur when negative-polarity breakdown processes reach into positive charge regions versus positive breakdown processes reaching into negative charge regions, and thus, higher concentrations of VHF sources are typically observed in positive charge regions (e.g., Thomas et al., 2001; Wiens et al., 2005). In Figure 5c, we note that the higher concentration of LMA sources is seen between approximately 12–14 km altitude, with a lower concentration at altitudes of 8–12 km. The altitudes of the lower concentration of LMA sources thus coincide with the high-reflectivity column shown in Figure 7, suggesting that the high-reflectivity column is composed of negatively charged graupel. From the above discussion we conclude that this TGF occurred temporally and spatially very close to the beginning of a flash in which a negatively charged leader extended upward from the main negative to the upper positive cloud charge region. Based on the available data, we cannot, however, confirm whether any CG strokes occurred during this flash.

5. Discussion

In some previous studies (e.g., Briggs et al., 2010; Connaughton et al., 2010, 2013) that examine TGFs and associated RF pulses reported by WWLLN, the TGF peak-time is used rather than the start-time when correlating with RF pulses because WWLLN reports the time of the peak radiated power of sferics (Connaughton et al., 2010). In this study we use the TGF's start-time because the start-time of TGF-associated RF pulses was available from the NLDN. As discussed in section 3, the RF pulses that occurred almost simultaneously with TGFs in our data set had median NLDN-estimated peak current that was significantly higher, and median rise time and peak-to-zero time that were significantly longer than the corresponding median values of these parameters for RF pulses that were not simultaneous with TGFs (but occurred within 5 ms of one). Additionally, from Table 1, we see that the majority (16 out of 22 or 73%) of these pulses had start-times that followed the corresponding TGF's photon flux start-time. We speculate that these RF pulses are signatures of either the relativistic electron avalanches associated with TGFs or currents traveling in conductive paths

preconditioned by TGF-associated relativistic electron beams between cloud charge regions of opposite polarity. Interestingly, the latter hypothesis is consistent with the observation that most NLDN-reported RF pulses in our relatively small data set start after the Fermi-reported TGF photon flux. Finally, the ratio of the initial peak to opposite polarity overshoot for the magnetic radiation field pulses ranged from 0.49 to 3.9, indicating their bipolar wave shape. This measure of the pulse shape, in conjunction with parameters such as current propagation speed, can be used to make inferences about the characteristics of the path of the source current. For example, in the case of compact intracloud discharges (CIDs) the bipolar radiation field pulse is likely due to a unipolar source current traveling over a relatively short channel length of few hundred meters (e.g., Nag, Rakov, & Cramer, 2011; Nag & Rakov, 2010).

Regardless of the origin of these pulses, the direction and polarity of the charge transferred during the transient process would determine the initial polarity of the RF-pulse radiation field waveform measured at ground. All previous studies (e.g., Cummer et al., 2005; Shao et al., 2010; Stanley et al., 2006), to the best of our knowledge, have reported the polarity of TGF-associated IC or CG lightning to be positive. For the TGFs in our data set, 27% had simultaneous RF pulses with NLDN-reported negative-initial polarity. As discussed in section 2, it is possible that the initial-polarity estimation for TGF RF signatures provided by the NLDN is affected by its measurement system and hence not indicative of the direction of charge motion. Alternatively, negative initial-polarity pulses associated with TGFs could indicate that these TGFs are due to downward electron avalanches, which are being detected by the GBM from above. In this case, their GBM-recorded signatures are expected to be much weaker than those of the upward directed TGFs, which produce positive RF pulses. In our data, we find that the GBM photon counts range from 9 to 34 with a median of 17 for TGFs with positive polarity NLDN pulses and from 11 to 19 with a median of 13 for TGFs with negative polarity NLDN pulses. However, our data set is not large enough to provide statistically reliable confirmation of photon-count differences between NLDN-reported positive versus negative polarity events. Of course, the TGF "brightness" at spacecraft altitude strongly depends on the horizontal distance between the TGF-source and the spacecraft-nadir and also the TGF source-altitude. If downward directed TGFs occur between the negative screening layer and upper positive cloud charge region, they will be at altitudes above upward directed TGFs and hence at shorter distances from the GBM. This might contribute, at least in part, toward "compensating" their signal strengths (relative to upward directed TGFs) detected by the GBM. In our data set, the median NLDN-estimated peak current for positive initial-polarity RF pulses occurring simultaneously with TGFs is 31 kA versus 25 kA for negative initial-polarity pulses. The median threshold-to-peak rise time is 14 μs for positive pulses versus 11 μs for negative pulses. Our data set is not large enough to make robust conclusions about the differences in characteristics of RF pulses occurring simultaneously with TGFs having positive versus negative initial-polarities. A detailed characterization of TGF-associated RF pulse signatures measured using wideband measurement systems is needed to shed more light on the issue of polarity of TGF-associated RF pulses.

In our data set, 77% of the simultaneous RF pulses had NLDN-estimated peak currents less than 50 kA and 50% had peak currents less than 25 kA. The minimum and median peak currents were 13 and 26 kA, respectively. This indicates that TGF emissions can be associated with moderate peak current (or peak amplitude) processes. For comparison, the median peak current for first return strokes in natural CG lightning is around 30 kA (Rakov & Uman, 2003). Shao et al. (2010) measured RF pulses (sferics) using the Los Alamos Sferic Array (LASA) for nine TGFs reported by RHESSI and estimated the peak currents of these events to range from 3 to 19 kA, which is mostly lower than the peak currents in our data set. Of course, a subset of TGFs are associated with discharges having very high ($>$150 kA) NLDN-estimated peak currents such as those reported by Lyu et al. (2016) and can produce "energetic in-cloud pulses". Only one 4% of our TGF-associated pulses had peak current greater than 200 kA, and four (17%) had peak currents greater than 100 kA. Note that, the NLDN uses an empirical field-to-current conversion equation calibrated to the transmission line model for CG return strokes to estimate peak currents (see e.g., Nag, Rakov, & Cramer, 2011). The median error of these peak current estimates obtained using rocket-triggered lightning peak currents as ground-truth is around 15% (e.g., Nag, Mallick, et al., 2011). These estimates are valid for return strokes with vertical lightning channels that are several kilometers long and are likely to be underestimates for discharges with smaller spatial extents. For example, Nag, Rakov, and Crame (2011) show, using a Hertzian dipole approximation for (CID) channels, that the NLDN underestimated the peak currents for CIDs in their data set, on average by a factor of about 2 to 5, depending upon the length of the CID

channels. Hence, assuming that the spatial extents of the TGF-associated discharges that produce these RF pulses are relatively small (about a kilometer or less), it is likely that their NLDN-estimated peak currents are underestimates.

We observed that TGF09 (discussed in section 4) occurred toward the beginning of a flash that later transferred charge between the main negative and upper positive charge regions. While the NLDN reported two "CG strokes" very close in time to this TGF, the LMA data do not show any VHF sources below about 4 km altitude. Observations of TGFs following CG strokes in rocket-triggered lightning have been reported by Dwyer et al. (2004) and Hare et al. (2016) and in natural lightning by Tran et al. (2015). TGFs have also been observed to occur during the initial stage of cloud lightning flashes (e.g., Lu et al., 2010; Shao et al., 2010).

Finally, the LMA geolocated a relatively high-power (20 dBW) VHF source at an altitude of 25 km occurring 101 μs after the start-time of TGF09 reported by GBM. This characteristic of TGF09 was also reported by Mailyan et al. (2017) and Lyu et al. (2017, 2018). The poor LMA-geolocation-quality of this high-power source could indicate that it was nonimpulsive and produced continuous VHF radiation, causing different LMA stations to detect slightly different peaks in the VHF signal, resulting in mislocation. High-power sources associated with other TGFs have not been reported before with microsecond precision. It is currently unknown whether all TGFs are associated with high-power VHF radiation. In this regard, it is interesting to note that CIDs produce relatively short duration (typically 10–30 μs) RF pulses along with high-power VHF radiation (e.g., Nag et al., 2010). CIDs with LMA-estimated peak VHF powers of about 50 dBW have been reported by Rison et al. (2016), which is 30 dBW larger than the peak power of the VHF source accompanying TGF09.

6. Summary

We examined the characteristics of magnetic field waveforms of RF pulses geolocated by the NLDN associated with 44 TGFs reported by the Fermi-GBM between January 2014 and July 2016. There were 61 such NLDN-reported RF pulses of which 23 pulses occurred almost simultaneously (within 200 μs) with 22 TGFs. Note that two NLDN-reported pulses occurred 5.0 μs before and 22 μs after the start-time of one of the TGFs. The median peak current for pulses that were simultaneous with TGFs was 26 kA versus 11 kA for pulses that were not simultaneous with TGFs (but occurred within 5 ms of one). The medians of the threshold-to-peak rise time and peak-to-zero time for the simultaneous pulses were about a factor of 4 and 3 longer, respectively, than those for nonsimultaneous pulses. While the majority of the simultaneous RF pulses had positive initial polarity, 27% had negative initial polarity. To the best of our knowledge, all previous studies have reported the polarity of TGF-associated IC or CG lightning to be positive. The exact nature of these NLDN-reported negative polarity RF signatures remains unknown, and a detailed characterization of TGF-associated RF pulse signatures measured using wideband measurement systems is needed to address this issue. We speculate that these RF pulses are signatures of either the relativistic electron avalanches associated with TGFs or currents traveling in conductive paths preconditioned by TGF-associated relativistic electron beams between cloud charge regions of opposite polarity.

One of the TGFs in our data set that occurred on 4 September 2015 was located about 10 km south-east of Tampa, Florida, a region covered by the KSC LMA. From our analysis of LMA, NLDN, and NEXRAD data we concluded that this TGF occurred temporally and spatially very close to the beginning of a flash in which a negatively leader extended upward from the main negative to the upper positive charge region. The LMA geolocated a relatively high-power (20 dBW) VHF source occurring 101 μs after the TGF start-time at an altitude of 25 km, but it is likely that the LMA estimated location (including the altitude) is somewhat unreliable due to the TGF-associated flash being relatively far (roughly 180 km) from the KSC LMA and also due to the probably continuous (nonimpulsive) VHF radiation from this source.

Acknowledgments
The authors would like to thank J. Wilson and R. Brown for the KSC LMA data, R. Holzworth and J. Brundell for the WWLLN data, and Vaisala Inc. for the NLDN and GLD360 data. The authors are thankful for insightful comments from S. Lazarus, A. Nina, and an anonymous reviewer. The Fermi-GBM TGF data are available at http://fermi.gsfc.nasa.gov/ssc/data/access/gbm/tgf/. The sounding data are available from the University of Wyoming (http://weather.uwyo.edu/upperair/sounding.html). The NEXRAD data were obtained from the NOAA National Climate Data Center (http://www.ncdc.noaa.gov). The NLDN/GLD360 data used in this paper can be accessed by contacting A. Nag (anag@fit.edu). This work was supported in part by AFOSR grant FA9550-16-1-0396.

References

Boccippio, D. J., Heckman, S., & Goodman, S. (2001). A diagnostic analysis of the Kennedy Space Center LDAR network: 1. Data characteristics. *Journal of Geophysical Research*, *106*(D5), 4769–4786.

Bowers, G. S., Smith, D. M., Martinez-McKinney, G. F., Kamogawa, M., Cummer, S. A., Dwyer, J. R., et al. (2017). Gamma ray signatures of neutrons from a terrestrial gamma ray flash. *Geophysical Research Letters*, *44*, 10,063–10,070. https://doi.org/10.1002/2017GL075071

Briggs, M., Fishman, G., Connaughton, V., Bhat, P. N., Paciesas, W., Preece, R., et al. (2010). First results on terrestrial gamma ray flashes from the Fermi Gamma-ray Burst Monitor. *Journal of Geophysical Research*, *115*, D16107. https://doi.org/10.1029/2009JA015242

Briggs, M. S., Xiong, S., Connaughton, V., Tierney, D., Fitzpatrick, G., Foley, S., et al. (2013). Terrestrial gamma-ray flashes in the Fermi era: Improved observations and analysis methods. *Journal of Geophysical Research: Space Physics*, *118*, 3805–3830. https://doi.org/10.1002/jgra.50205

Carlson, B. E., Lehtinen, N. G., & Inan, U. S. (2009). Terrestrial gamma ray flash production by lightning current pulses. *Journal of Geophysical Research*, *114*, A00E08. https://doi.org/10.1029/2009JA014531

Celestin, S., & Pasko, V. P. (2011). Energy and fluxes of thermal runaway electrons produced by exponential growth of streamers during the stepping of lightning leaders and in transient luminous events. *Journal of Geophysical Research*, *116*, A03315. https://doi.org/10.1029/2010JA016260

Chronis, T., Briggs, M. S., Priftis, G., Connaughton, V., Brundell, J., Holzworth, R., et al. (2015). Characteristics of thunderstorms that produce terrestrial gamma ray flashes. *Bulletin of the American Meteorological Society*, *97*, 639–653.

Connaughton, V., Briggs, M., Holzworth, R., Hutchins, M., Fishman, G., Wilson-Hodge, C., et al. (2010). Associations between Fermi Gamma-ray Burst Monitor terrestrial gamma ray flashes and sferics from the World Wide Lightning Location Network. *Journal of Geophysical Research*, *115*, A12307. https://doi.org/10.1029/2010JA015681

Connaughton, V., Briggs, M. S., Xiong, S., Dwyer, J. R., Hutchins, M. L., Grove, J. E., et al. (2013). Radio signals from electron beams in terrestrial gamma-ray flashes. *Journal of Geophysical Research: Space Physics*, *118*, 2313–2320. https://doi.org/10.1029/2012JA018288

Cummer, S. A., Briggs, M. S., Dwyer, J. R., Xiong, S., Connaughton, V., Fishman, G. J., et al. (2014). The source altitude, electric current, and intrinsic brightness of terrestrial gamma ray flashes. *Geophysical Research Letters*, *41*, 8586–8593. https://doi.org/10.1002/2014GL062196

Cummer, S. A., Lu, G., Briggs, M. S., Connaughton, V., Xiong, S., Fishman, G. J., & Dwyer, J. R. (2011). The lightning-TGF relationship on microsecond timescales. *Geophysical Research Letters*, *38*, L14810. https://doi.org/10.1029/2011GL048099

Cummer, S. A., Zhai, Y., Hu, W., Smith, D. M., Lopez, L. I., & Stanley, M. A. (2005). Measurements and implications of the relationship between lightning and terrestrial gamma ray flashes. *Geophysical Research Letters*, *32*, L08811. https://doi.org/10.1029/2005GL022778

Cummins, K., & Murphy, M. (2009). An overview of lightning locating systems: History, techniques, and data uses, with an in-depth look at the US NLDN. *IEEE Transactions on Electromagnetic Compatibility*, *51*(3), 499–518. https://doi.org/10.1109/TEMC.2009.2023450

Cummins, K. L., Honma, N., Pifer, A. E., Rogers, T., & Tatsumi, M. (2012). Improved detection of winter lightning in the Tohuku region of Japan using Vaisala's LS700x technology. *The Institute of Electrical Engineers of Japan*, *132*(6), 529–535. https://doi.org/10.1541/ieejpes.123.529

Dwyer, J. (2003). A fundamental limit on electric fields in air. *Geophysical Research Letters*, *30*(20), 2055. https://doi.org/10.1029/2003GL017781

Dwyer, J., & Smith, D. (2005). A comparison between Monte Carlo simulations of run-away breakdown and terrestrial gamma-ray flash observations. *Geophysical Research Letters*, *32*, L22804. https://doi.org/10.1029/2005GL023848

Dwyer, J. R. (2012). The relativistic feedback discharge model of terrestrial gamma ray flashes. *Journal of Geophysical Research*, *117*, A02308. https://doi.org/10.1029/2011JA017160

Dwyer, J. R., & Cummer, S. A. (2013). Radio emissions from terrestrial gamma-ray flashes. *Journal of Geophysical Research: Space Physics*, *118*, 3769–3790. https://doi.org/10.1002/jgra.50188

Dwyer, J. R., Rassoul, H. K., al-Dayeh, M., Caraway, L., Wright, B., Chrest, A., et al. (2004). A ground level gamma-ray burst observed in association with rocket-triggered lightning. *Geophysical Research Letters*, *31*(5), L05119. https://doi.org/10.1029/2003GL018771

Dwyer, J. R., Schaal, M. M., Cramer, E., Arabshahi, S., Liu, N., Rassoul, H. K., et al. (2012). Observation of a gamma-ray flash at ground level in association with a cloud-to-ground lightning return stroke. *Journal of Geophysical Research*, *117*, A10303. https://doi.org/10.1029/2012JA017810

Enoto, T., Wada, Y., Furuta, Y., Nakazawa, K., Yuasa, T., Okuda, K., et al. (2017). Photonuclear reactions triggered by lightning discharge. *Nature*, *551*(7681), 481.

Fishman, G. J., Bhat, P. N., Mallozzi, R., Horack, J. M., Koshut, T., Kouveliotou, C., et al. (1994). Discovery of intense gamma-ray flashes of atmospheric origin. *Science*, *59*, 1313–1316.

Gjesteland, T., Østgaard, N., Laviola, S., Miglietta, M. M., Arnone, E., Marisaldi, M., et al. (2015). Observation of intrinsically bright terrestrial gamma ray flashes from the Mediterranean basin. *Journal of Geophysical Research: Atmospheres*, *120*, 12,143–12,156. https://doi.org/10.1002/2015JD023704

Gurevich, A., Milikh, G., & Roussel-Dupre, R. (1992). Runaway electron mechanism of air breakdown and preconditioning during a thunderstorm. *Physics Letters A*, *165*(5), 463–468.

Hall, M. P., Goddard, J. W., & Cherry, S. M. (1984). Identification of hydrometeors and other targets by dual-polarization radar. *Radio Science*, *19*(1), 132–140.

Hare, B. M., Uman, M. A., Dwyer, J. R., Jordan, D. M., Biggerstaff, M. I., Caicedo, J. A., et al. (2016). Ground-level observation of a terrestrial gamma ray flash initiated by a triggered lightning. *Journal of Geophysical Research: Atmospheres*, *121*, 6511–6533. https://doi.org/10.1002/2015JD024426

Honma, N., Cummins, K. L., Murphy, M. J., Pifer, A. E., & Rogers, T. S. (2013). Improved lightning locations in the Tohoku Region of Japan using propagation and waveform onset corrections. *IEEJ Transactions on Power and Energy*, *133*(2), 195–202. https://doi.org/10.1541/ieejpes.133.195

Inan, U. S., & Lehtinen, N. G. (2005). Production of terrestrial gamma-ray flashes by an electromagnetic pulse from a lightning return stroke. *Geophysical Research Letters*, *32*, L19818. https://doi.org/10.1029/2005GL023702

Inan, U. S., Reising, S. C., Fishman, G. J., & Horack, J. M. (1996). On the association of terrestrial gamma-ray bursts with lightning and implications for sprites. *Geophysical Research Letters*, *23*(9), 1017–1020.

Krehbiel, P. R., Thomas, R. J., Rison, W., Hamlin, T., Harlin, J., & Davis, M. (2000). GPS-based mapping system reveals lightning inside storms. *Eos, Transactions American Geophysical Union*, *81*(3), 21–25.

Lin, Y. T., Uman, M. A., Tiller, J. A., Brantley, R. D., Beasley, W. H., Krider, E. P., & Weidman, C. D. (1979). Characterization of lightning return stroke electric and magnetic fields from simultaneous two-station measurements. *Journal of Geophysical Research*, *84*(C10), 6307–6314. https://doi.org/10.1029/JC084iC10p06307

Lu, G., Blakeslee, R. J., Li, J., Smith, D. M., Shao, X.-M., McCaul, E. W., et al. (2010). Lightning mapping observation of a terrestrial gamma-ray flash. *Geophysical Research Letters*, *37*, L11806. https://doi.org/10.1029/2010GL043494

Lyu, F., Cummer, S. A., Krehbiel, P. R., Rison, W., Briggs, M. S., Cramer, E., et al. (2018). Very high frequency radio emissions associated with the production of terrestrial gamma-ray flashes. *Geophysical Research Letters*, *45*, 2097–2105. https://doi.org/10.1002/2018GL077102

Lyu, F., Cummer, S., Krehbiel, P., Rison, W., Briggs, M., Cramer, E., et al. (2017). Terrestrial gamma ray flashes observed by Fermi, lightning mapping arrays and distant ground based radio sensors, Abstract AE31A-02 presented at 2017 Fall Meeting, AGU, New Orleans, LA, 11–15 Dec.

Lyu, F., Cummer, S. A., Briggs, M., Marisaldi, M., Blakeslee, R. J., Bruning, E., et al. (2016). Ground detection of terrestrial gamma ray flashes from distant radio signals. *Geophysical Research Letters*, *43*, 8728–8734. https://doi.org/10.1002/2016GL070154

Mailyan, B., Briggs, M., Cramer, E., Fitzpatrick, G., Roberts, O., Stanbro, M., et al. (2016). The spectroscopy of individual terrestrial gamma-ray flashes: Constraining the source properties. *Journal of Geophysical Research: Space Physics*, *121*, 11,346–11,363. https://doi.org/10.1002/2016JA022702

Mailyan, B., Nag, A., Murphy, M., Briggs, M., Dwyer, J., Cramer, E., Stanbro, M., et al. (2017). Characteristics of NLDN-reported radio frequency emissions associated with terrestrial famma-ray flashes, Abstract AE31A-04 presented at 2017 Fall Meeting, AGU, New Orleans, LA, 11–15 Dec.

Mallick, S., Rakov, V., Ngin, T., Gamerota, W., Pilkey, J., Hill, J., et al. (2014). Evaluation of the WWLLN performance characteristics using rocket-triggered lightning data, in Intl. Conf. on Grounding and Earthing/6th Intl. Conf. on Lightning Physics and Effects.

Marisaldi, M., Fuschino, F., Labanti, C., Galli, M., Longo, F., Del Monte, E., et al. (2010). Detection of terrestrial gamma ray flashes up to 40 MeV by the AGILE satellite. *Journal of Geophysical Research*, *115*, A00E13. https://doi.org/10.1029/2009JA014502

Meegan, C., Lichti, G., Bhat, P. N., Bissaldi, E., Briggs, M. S., Connaughton, V., et al. (2009). The Fermi Gamma-ray Burst Monitor. *The Astrophysical Journal*, *702*(1), 791.

Mezentsev, A., Østgaard, N., Gjesteland, T., Albrechtsen, K., Lehtinen, N., Marisaldi, M., et al. (2016). Radio emissions from double RHESSI TGFs. *Journal of Geophysical Research: Atmospheres*, *121*, 8006–8022. https://doi.org/10.1002/2016JD025111

Moss, G. D., Pasko, V. P., Liu, N., & Veronis, G. (2006). Monte Carlo model for analysis of thermal runaway electrons in streamer tips in transient luminous events and streamer zones of lightning leaders. *Journal of Geophysical Research*, 111, A02307. https://doi.org/10.1029/2005JA011350

Murphy, M., & Nag, A. (2015). Cloud lightning performance and climatology of the U.S. based on the upgraded U.S. National Lightning Detection Network, in Seventh Conference on the Meteorological Applications of Lightning Data, paper 8.4, Am. Meteorol. Soc., Phoenix, Ariz., 4–8 Jan.

Nag, A., Mallick, S., Rakov, V. A., Howard, J. S., Biagi, C. J., Hill, J. D., et al. (2011). Evaluation of U.S. National Lightning Detection Network performance characteristics using rocket-triggered lightning data acquired in 2004–2009. *Journal of Geophysical Research*, *116*, D02123. https://doi.org/10.1029/2010JD014929

Nag, A., Murphy, M. J., Schulz, W., & Cummins, K. L. (2015). Lightning locating systems: Insights on characteristics and validation techniques. *Earth and Space Science*, *2*, 65–93. https://doi.org/10.1002/2014EA000051

Nag, A., Rakov, V., & Cramer, J. (2011). Remote measurements of currents in cloud lightning discharges. *IEEE Transactions on Electromagnetic Compatibility*, *53*(2), 407–413.

Nag, A., & Rakov, V. A. (2010). Compact intracloud lightning discharges: 1. Mechanism of electromagnetic radiation and modeling. *Journal of Geophysical Research*, *115*, D20102. https://doi.org/10.1029/2010JD014235

Nag, A., Rakov, V. A., Tsalikis, D., & Cramer, J. A. (2010). On phenomenology of compact intracloud lightning discharges. *Journal of Geophysical Research*, *115*, D14115. https://doi.org/10.1029/2009JD012957

Park, H., Ryzhkov, A. V., Zrnic, D. S., & Kim, K.-E. (2009). The hydrometeor classification algorithm for the polarimetric WSR-88D: Description and application to an MCS. *Weather and Forecasting*, *24*, 730–748.

Rakov, V. A., & Uman, M. A. (2003). *Lightning: Physics and effects*. New York: Cambridge Univ. Press.

Rison, W., Krehbiel, P. R., Stock, M. G., Edens, H. E., Shao, X.-M., Thomas, R. J., et al. (2016). Observations of narrow bipolar events reveal how lightning is initiated in thunderstorms. *Nature Communications*, *7*, 10721.

Roberts, O. J., Fitzpatrick, G., Stanbro, M., McBreen, S., Briggs, M. S., Holzworth, R. H., et al. (2018). The first Fermi-GBM terrestrial gamma ray flash catalog. *Journal of Geophysical Research: Space Physics*, *123*, 4381–4401. https://doi.org/10.1029/2017JA024837

Saunders, C. P. R. (2008). Charge separation mechanisms in clouds. *Space Science Reviews*, *137*, 335–353. https://doi.org/10.1007/s11214-008-9345-0

Shao, X.-M., Hamlin, T., & Smith, D. M. (2010). A closer examination of terrestrial gamma-ray flash-related lightning processes. *Journal of Geophysical Research*, *115*, A00E30. https://doi.org/10.1029/2009JA014835

Smith, D. M., Buzbee, P., Kelley, N. A., Infanger, A., Holzworth, R. H., & Dwyer, J. R. (2016). The rarity of terrestrial gamma-ray flashes: 2. RHESSI stacking analysis. *Journal of Geophysical Research: Atmosphere*, *121*, 11,382–11,404. https://doi.org/10.1002/2016JD025395

Smith, D. M., Dwyer, J. R., Hazelton, B. J., Grefenstette, B. W., Martinez-McKinney, G. F. M., Zhang, Z. Y., et al. (2011). A terrestrial gamma ray flash observed from an aircraft. *Journal of Geophysical Research*, *116*, D20124. https://doi.org/10.1029/2011JD016252

Smith, D. M., Lopez, L. I., Lin, R. P., & Barrington-Leigh, C. P. (2005). Terrestrial gamma-ray flashes observed up to 20 MeV. *Science*, *307*, 1085–1088.

Stanley, M. A., Shao, X.-M., Smith, D. M., Lopez, L. I., Pongratz, M. B., Harlin, J. D., et al. (2006). A link between terrestrial gamma-ray flashes and intracloud lightning discharges. *Geophysical Research Letters*, *33*, L06803. https://doi.org/10.1029/2005GL025537

Thomas, R. J., Krehbiel, P. R., Rison, W., Hamlin, T., Harlin, J., & Shown, D. (2001). Observations of VHF source powers radiated by lightning. *Geophysical Research Letters*, *28*(1), 143–146.

Thomas, R. J., Krehbiel, P. R., Rison, W., Hunyady, S. J., Winn, W. P., Hamlin, T., & Harlin, J. (2004). Accuracy of the Lightning Mapping Array. *Journal of Geophysical Research*, *109*, D14207. https://doi.org/10.1029/2004JD004549

Tran, M. D., Rakov, V. A., Mallick, S., Dwyer, J. R., Nagc, A., & Heckman, S. (2015). A terrestrial gamma-ray flash recorded at the Lightning Observatory in Gainesville, Florida. *Journal of Atmospheric and Solar - Terrestrial Physics*, *136*, 86–93. https://doi.org/10.1016/j.jastp.2015.10.010

Wiens, K. C., Rutledge, S. A., & Tessendorf, S. A. (2005). The 29 June 2000 supercell observed during STEPS. Part II: Lightning and charge structure. *Journal of the Atmospheric Sciences*, *62*, 4151–4177.

Williams, E., Boldi, R., Bor, J., Satori, G., Price, C., Greenberg, E., et al. (2006). Lightning flashes conducive to the production and escape of gamma radiation to space. *Journal of Geophysical Research*, *111*, D16209. https://doi.org/10.1029/2005JD006447

Zhu, Y., Rakov, V. A., Tran, M. D., & Nag, A. (2016a). Study of NLDN responses to cloud discharge activity based on ground-truth data acquired at the LOG, in 24th International Lightning Detection Conference & 6th International Lightning Meteorology Conference, Vaisala Inc., San Diego, Calif.

Zhu, Y., Rakov, V. A., Tran, M. D., & Nag, A. (2016b). A study of National Lightning Detection Network responses to natural lightning based on ground truth data acquired at LOG with emphasis on cloud discharge activity. *Journal of Geophysical Research: Atmospheres*, *121*, 14,651–14,660. https://doi.org/10.1002/2016JD025574